

synax: A Differentiable and GPU-accelerated Synchrotron Simulation Package

KANGNING DIAO ^{1,2} ZACK LI ² RICHARD D.P. GRUMITT ¹ AND YI MAO ¹


¹*Department of Astronomy, Tsinghua University, Beijing, 100084, China*

²*Berkeley Center for Cosmological Physics, University of California, Berkeley, CA 94720, United States*

(Received XXX; Revised YYY; Accepted ZZZ)

Submitted to ApJS

ABSTRACT

We introduce **synax** , a novel library for automatically differentiable simulation of Galactic synchrotron emission. Built on the JAX framework, **synax** leverages JAX’s capabilities, including batch acceleration, just-in-time compilation, and hardware-specific optimizations (CPU, GPU, TPU). Crucially, **synax** uses JAX’s automatic differentiation (AD) mechanism, enabling precise computation of derivatives with respect to any model parameters. This feature facilitates powerful inference algorithms, such as Hamiltonian Monte Carlo (HMC) and gradient-based optimization, which enables inference over models that would otherwise be computationally prohibitive. In its initial release, **synax** supports synchrotron intensity and polarization calculations down to GHz frequencies, alongside several models of the Galactic magnetic field (GMF), cosmic ray (CR) spectra, and thermal electron density fields. We demonstrate the transformative potential of AD for tasks involving full posterior inference using gradient-based techniques or Maximum Likelihood Estimation (MLE) optimization. Notably, we show that GPU acceleration brings a twenty-fold enhancement in efficiency, while HMC achieves a two-fold improvement over standard random walk Metropolis-Hastings (RWMH) when performing inference over a four-parameter test model. HMC still works on a more complex, 16-parameter model while RWMH fails to converge. Additionally, we showcase the application of **synax** in optimizing the GMF based on the Haslam 408 MHz map, achieving residuals with a standard deviation below 1 K.

Keywords: Synchrotron emission (856) — Galaxy magnetic fields(604) — Radio astronomy(1338) — Astrophysical simulations(1857)

1. INTRODUCTION

Galactic synchrotron emission dominates the low-frequency radio sky, spanning frequencies from MHz to GHz, and obscures cosmological signals, including those from the cosmic microwave background (CMB; Krachmalnicoff et al. 2018; Jones et al. 2018; Rubiño-Martín et al. 2023), the 21 cm line (Liu & Shaw 2020), and other line intensity measurements (e.g. Gong et al. 2014; Maniyar et al. 2023). This emission originates from the interaction between cosmic ray (CR) electrons and the Galactic magnetic field (GMF), with polarization altered as a result of Faraday rotation in the presence of the GMF and thermal electrons (Rybicki & Lightman 1986). Consequently, while mitigating synchrotron emission

is essential for extracting cosmological signals, the emission itself serves as a probe for the structure of the Galactic interstellar medium (ISM) and CR transport processes (e.g. Unger & Farrar 2024).

During the past decades, several simulation packages have been developed to model Galactic synchrotron emission, including **hammurabi** (Waelkens et al. 2009; Wang et al. 2020) and **ULSA** (Cong et al. 2021). **hammurabi**, when combined with models of the GMF (Bennett et al. 2003; Jansson & Farrar 2012), CRs (Bennett et al. 2003), and thermal electrons (Yao et al. 2017), has successfully reproduced the large-scale components of the Galactic disk but has struggled to capture finer structures. Furthermore, **hammurabi** has been employed in simulation-based inference to study magnetic fields in astrophysical contexts, ranging from supernova remnants (West et al. 2017) to the entire Galaxy (Jansson & Farrar 2012; Planck Collaboration et al. 2016a). **ULSA** extends these

capabilities by incorporating free-free emission and absorption, enabling precise simulations down to 1 MHz. Utilizing ULAS, Markov chain Monte Carlo (MCMC) methods have been applied to infer the local three-dimensional distribution of thermal electrons (Cong et al. 2022).

However, synchrotron simulations remain computationally demanding, as they require integration along numerous sightlines with fine resolution. These operations can be highly parallelized because of the independence between different sightlines. Recently, JAX (DeepMind et al. 2020) has emerged as a multiplatform computing framework, supporting CPUs, GPUs, TPUs, and offering automatic differentiation (AD). GPUs, designed for parallel computation, are particularly well suited for synchrotron simulations. Moreover, AD provides access to gradients, allowing more powerful sampling and optimization algorithms, which are crucial to conducting inference on more complex models (Gelman et al. 1997; Beskos et al. 2013).

In this work, we present *synax*, a synchrotron simulation package powered by JAX. The code is implemented in a parallelized manner, significantly accelerating sampling and optimization algorithms. While modeling complex and turbulent fields are challenging tasks, our code allows for a 3D grid representation of the fields to better characterize the full 3D structure. Here, we assess the accuracy and performance of using a coarse 3D grid as the input field and estimate the corresponding error budget.

This paper is organized as follows. In Section 2, we describe the theory and formalism for computing synchrotron emission. In Section 3, we present examples of fast gradient-based inference algorithms, which demonstrate the capabilities of *synax*. We discuss the error budget and performance concerning integration points and demonstrate sampling over a 16-parameter model and optimization of the GMF based on the 408 MHz Haslam map (Remazeilles et al. 2015) in Section 4. Finally, we summarize our findings in Section 5.

2. METHOD

In this section, we follow Rybicki & Lightman (1986) and describe the physical processes and the numerical techniques used to compute the synchrotron emission maps.

2.1. Synchrotron Intensity

Galactic synchrotron emission is caused by the spiraling of relativistic charges in the GMF. We assume that CR electrons generated by supernova explosions dominate the population of Galactic relativistic charges, and these electrons subsequently experience shock acceleration. We further simplify the problem by assuming an isotropic velocity distribution for CR electrons, which has been measured with high accuracy to be the case at our location in the Galaxy (Yan & Lazarian 2008). A full CR spectrum treatment will be addressed in future work to better simulate the emission.

The CR electron spectrum is typically modeled as a power law with a spectral index α . This widely used simplification is supported by the theory of shock acceleration (Drury 1983) and has been broadly adopted in previous work (Cong et al. 2021; Waelkens et al. 2009; Wang et al. 2020). This assumption has also been successfully applied to CMB foreground subtraction (Planck Collaboration et al. 2020; Eriksen et al. 2008; Planck Collaboration et al. 2016b) and corroborated by measurements of the CR electron spectrum on Earth (e.g. Adriani et al. 2011; Gaisser et al. 2013). While both observations and advanced simulations have shown that the power-law assumption is inadequate for representing the entire spectrum (e.g. Strong et al. 2007), accurately accounting for the full spectrum is significantly more time-consuming. Therefore, we adopt the assumption of power-law spectrum for simplicity in this work in favor of a balance between accuracy and computational efficiency, leaving a more detailed treatment for future work.

Given the physical processes and assumptions, the specific intensity of synchrotron emission $I(\nu, \hat{\mathbf{n}})$ at given frequency ν and along the line-of-sight (LOS) direction $\hat{\mathbf{n}}$ can be given by

$$I(\nu, \hat{\mathbf{n}}) = \int_0^\infty j_1(\nu, r' \hat{\mathbf{n}} + \mathbf{r}_{\text{obs}}) dr', \quad (1)$$

where r' is the distance of a field point to the observer on Earth, $\mathbf{r}_{\text{obs}} = (-8.3, 0.0, 0.006)$ kpc is the distance vector from the Galactic center to the Earth. Here, $j_1(\nu, \mathbf{r})$ is the emissivity of the synchrotron specific intensity, where $\mathbf{r} = r' \hat{\mathbf{n}} + \mathbf{r}_{\text{obs}}$ is the distance vector from the Galactic center to the field point. The emissivity j_1 is given by

$$j_1(\nu, \mathbf{r}) = \frac{\sqrt{3} q_e^3 B_{\text{trans}}(\mathbf{r}) N_0(\mathbf{r})}{8\pi m_e c^2} \left(\frac{4\pi \nu m_e c}{3q_e B_{\text{trans}}(\mathbf{r})} \right)^{(1-\alpha)/2} \times \frac{2^{(\alpha+1)/2}}{\alpha+1} \Gamma\left(\frac{\alpha}{4} - \frac{1}{12}\right) \Gamma\left(\frac{\alpha}{4} + \frac{19}{12}\right). \quad (2)$$

The amplitude of the GMF transverse to the LOS direction is given by B_{trans} , q_e is the electron charge, m_e is the electron mass and c is the speed of light. We assume the high-energy CR electrons follow a power law $N(\gamma, \mathbf{r}) d\gamma = N_0(\mathbf{r}) \gamma^{-\alpha} d\gamma$, where $N_0(\mathbf{r})$ is the normalization factor and γ is the Lorentz factor.

2.2. Synchrotron Polarization

For synchrotron polarization, we focus on the specific intensity of polarization P . We further define the parameters Q and U , which describe the specific intensity of linear polarization, through $P = Q + iU$. The quantities $\{I, Q, U\}$ are related with the first three Stokes parameters $\{S_0, S_1, S_2\}$ by

$$S_0 = \int I d\Omega, \quad S_1 = \int Q d\Omega, \quad S_2 = \int U d\Omega \quad (3)$$

where Ω is the solid angle. The polarization P is given by

$$P(\nu, \hat{\mathbf{n}}) = \int_0^\infty j_P(\nu, r' \hat{\mathbf{n}} + \mathbf{r}_{\text{obs}}) e^{2i\chi(r' \hat{\mathbf{n}} + \mathbf{r}_{\text{obs}})} dr', \quad (4)$$

where j_P is the synchrotron polarized emissivity, given by

$$j_P(\nu, \mathbf{r}) = \frac{\sqrt{3} q_e^3 B_{\text{trans}}(\mathbf{r}) N_0(\mathbf{r})}{8\pi m_e c^2} \left(\frac{4\pi \nu m_e c}{3 q_e B_{\text{trans}}(\mathbf{r})} \right)^{(1-\alpha)/2} \times 2^{(\alpha-3)/2} \Gamma\left(\frac{\alpha}{4} - \frac{1}{12}\right) \Gamma\left(\frac{\alpha}{4} + \frac{7}{12}\right), \quad (5)$$

and $\chi(\mathbf{r})$ is the observed polarization angle of the polarized emission emitted at \mathbf{r} .

Synchrotron radiation undergoes Faraday rotation as it travels through a magnetized plasma, causing the polarization angle to vary with frequency. The polarization angle χ can be modeled as

$$\chi(\mathbf{r}) = \text{RM} \cdot \lambda^2 + \chi_0(\mathbf{r}), \quad (6)$$

where λ is the wavelength and the rotation measure (RM) quantifies the linear rate of change of the angle χ . RM, which depends on $\mathbf{r} = r' \hat{\mathbf{n}} + \mathbf{r}_{\text{obs}}$, can be calculated via

$$\text{RM} = \frac{q_e^3}{2\pi m_e^2 c^4} \int_0^{r'} n_e(r'' \hat{\mathbf{n}} + \mathbf{r}_{\text{obs}}) B_{\text{LOS}}(r'' \hat{\mathbf{n}} + \mathbf{r}_{\text{obs}}) dr'', \quad (7)$$

where n_e is the electron density and $B_{\text{LOS}} = \|\mathbf{B} \cdot \hat{\mathbf{n}}\|$ is the amplitude of the LOS component of the magnetic field.

The intrinsic polarization angle χ_0 is defined as (e.g. Wang et al. 2020)

$$\tan(\chi_0) = \frac{B_z \cos(b) - B_x \cos(l) \sin(b) - B_y \sin(l) \sin(b)}{B_y \sin(l) - B_x \cos(l)}. \quad (8)$$

Here (B_x, B_y, B_z) is the x, y and z -component of $\mathbf{B}(\mathbf{r})$ field, respectively, where the directions of axes are defined as in the Galactic coordinates, and l is the Galactic longitude and b is the Galactic latitude for the LOS as seen by the observer on Earth.

2.3. Integration

The input fields required when simulating synchrotron emission with *syntax* are :

1. 3D GMF $\mathbf{B}(\mathbf{r})$,
2. 3D thermal electron density distribution $n_e(\mathbf{r})$,
3. Normalizing factor of CR electron distribution $N_0(\mathbf{r})$,
4. Power-law index of the CR energy spectrum α .

We follow Bennett et al. (2003) and set the power law index $\alpha = 3$ throughout this paper unless otherwise noted.

Integration points

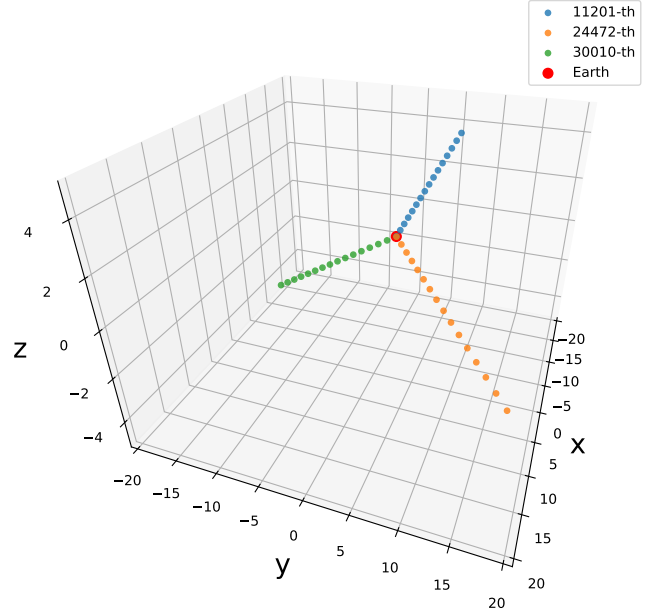


Figure 1. An illustration of the integration points along several sightlines with the number of integration points $N_{\text{int}} = 16$ in a box of length (40, 40, 10) kpc along the x, y, z direction, respectively. The legend shows the index of the sightline for an NSIDE = 64 healpix map, while the large red dot represents the observer on Earth.

For the fields $\{\mathbf{B}(\mathbf{r}), n_e(\mathbf{r}), N_0(\mathbf{r})\}$, *syntax* accepts a callable field generator function as input. This function can either be an analytical model or an interpolation function operating over 3D grids (hereafter 3D grids). To ensure consistency between 3D grids and analytical functions, we assume that all fields are confined within a 3D box of dimensions (l_x, l_y, l_z) centered at the Galactic center, with contributions from outside the box being considered negligible.

We begin by generating the coordinates for all integration points. For the i -th sightline in the healpix map, the coordinates $\{l_i, b_i\}$ are obtained using *healpy*. The intersection point between the sightline and the boundary of the 3D box is then calculated. The entire LOS from the observer to the boundary is uniformly divided into N_{int} segments with the segment length Δr_i , and the midpoint coordinates $\{\mathbf{r}_{i,n}\}$, where $n = 1, 2, \dots, N_{\text{int}}$, are computed for each segment. The field values $\{\mathbf{B}(\mathbf{r}_{i,n}), n_e(\mathbf{r}_{i,n}), N_0(\mathbf{r}_{i,n})\}$ are then evaluated at each of the midpoints. Figure 1 provides an illustration of the integration points along several sightlines. If an analytical function is provided for a field, its value at $\mathbf{r}_{i,n}$ is calculated analytically. Otherwise, we determine the field values using 3D linear interpolation, implemented with *Interpax*¹.

¹ <https://interpax.readthedocs.io/en/latest/>

With these field values, χ , j_I , and j_P can be computed at each $\mathbf{r}_{i,n}$ using Equations (2)-(8). Discretizing along the sightline and multiplying by the segment length Δr_i yields the specific intensities I , Q , and U ,

$$\begin{aligned} I(\nu, \hat{\mathbf{n}}_i) &= \sum_{n=1}^{N_{\text{int}}} j_I(\nu, \mathbf{r}_{i,n}) \Delta r_i, \\ Q(\nu, \hat{\mathbf{n}}_i) &= \sum_{n=1}^{N_{\text{int}}} j_P(\nu, \mathbf{r}_{i,n}) \cos(2\chi(\mathbf{r}_{i,n})) \Delta r_i, \\ U(\nu, \hat{\mathbf{n}}_i) &= \sum_{n=1}^{N_{\text{int}}} j_P(\nu, \mathbf{r}_{i,n}) \sin(2\chi(\mathbf{r}_{i,n})) \Delta r_i, \end{aligned} \quad (9)$$

2.4. Validation and Performance on a Toy Model

We first test our model on a simple scenario (Wang et al. 2020) at $\nu = 2.4$ GHz. In this model, the fields are homogeneous, $\mathbf{B}(\mathbf{r}) = (6 \times 10^{-6} \text{ gauss}, 0, 0)$, $n_e(\mathbf{r}) = 0.01 \text{ cm}^{-3}$, and $N_0(\mathbf{r}) = 4.01 \times 10^{-5} \text{ cm}^{-3}$ within a spherical region of the radius $R_0 = 4$ kpc of the Earth, and zero outside. (Note that these fields are not spherically symmetric with respect to the Galactic center.) In this case, the emission intensity before Faraday rotation $\{I, Q_0, U_0\}$ becomes:

$$\begin{aligned} I &= j_I R_0, \\ Q_0 &= j_P R_0 \cos(2\chi_0), \\ U_0 &= j_P R_0 \sin(2\chi_0), \end{aligned} \quad (10)$$

since j_I, j_P, χ_0 are constants along a sightline. The Q_0 and U_0 will be altered by

$$Q + iU = (Q_0 + iU_0) \int_0^{R_0} \frac{1}{R_0} e^{2i\lambda^2 r' n_e B_{\text{LOS}} q_e^3 / 2\pi m_e^2 c^4} dr' \quad (11)$$

Thus, $\{I, Q, U\}$ maps can be calculated analytically.

We then simulate the $\{I, Q, U\}$ maps with `synax`, and for this demonstration we specify $\text{NSIDE} = 64$ and $N_{\text{int}} = 1024$. The length of the box is $(40, 40, 10)$ kpc. We set the input as analytical functions and the results are shown in Figure 2. The typical scale of absolute residuals is below 1% of the signal scale, and the relative error, defined by $\epsilon_{\text{rel}} = 2(X_{\text{sim}} - X_{\text{ana}}) / (X_{\text{sim}} + X_{\text{ana}})$ where X_{sim} is the simulated map and X_{ana} is the analytical map, is also mostly at the percentage level, except for sightlines with field value very close to zero. We note that the residuals are all below 1 mK, suggesting that `synax` with function input has no significant bias with mK noise level observations.

Our code is based on JAX (DeepMind et al. 2020) and can run on multiple platforms including CPU, GPU, and TPU. `synax` uses ~ 300 ms to generate the emission map on an NVidia Tesla A100 after just-in-time (JIT) compilation. For comparison, it takes $\sim 30,000$ ms for the MPI-parallelized CPU-based code `hampyx` (Wang et al. 2020) to run with 64

threads on an AMD milan CPU, while it only integrates with 100 points along each sightline. `synax` obtains the same level of accuracy as `hampyx`, with the standard deviation of residuals for the $\{I, Q, U\}$ maps with `synax` being $\{1.6 \times 10^{-4}, 2.0 \times 10^{-4}, 2.0 \times 10^{-4}\}$, while with `hampyx` the standard deviation of residuals is $\{1.6 \times 10^{-5}, 5.6 \times 10^{-4}, 6.0 \times 10^{-4}\}$, respectively. `synax` gains $\gtrsim 100$ times improvement in wall clock time, along with access to the gradient with AD.

3. ACCELERATED INFERENCE WITH `synax`

In this section, we demonstrate the performance of `synax` when performing inference using gradient-based algorithms on two test cases. In the first example, we use the No-Turn sampler (NUTS; Hoffman & Gelman 2011), a variant of Hamiltonian Monte Carlo (HMC; see e.g. Betancourt 2017) to obtain the posterior distributions for model parameters. The sampler is implemented in Blackjax² (Cabezas et al. 2024). In the second example, we use gradient-based optimization on extremely high-dimensional 3D grids beyond sampling parameters of analytical models.

3.1. Model Setup

In our mock observation, we simulate the $\{Q, U\}$ maps with `synax`. The N_0 model here is the one adopted by WMAP (Drimmel & Spergel 2001; Page et al. 2007),

$$N_0(\mathbf{r}) = C_0 e^{-\rho/h_r} \text{sech}^2(z/h_z), \quad (12)$$

where $\mathbf{r} = (x, y, z)$ and $\rho = (x^2 + y^2)^{1/2}$. We fix the free parameter $h_r = 5$ kpc and $h_z = 1$ kpc, as the original WMAP parameter values. The value of C_0 is fixed by $N_{0,\text{Earth}} = 4.0 \times 10^{-5} \text{ cm}^{-3}$, consistent with the observations of 10 GeV electrons on Earth (e.g. Strong et al. 2007). The n_e model is the YMW16 model (Yao et al. 2017), a complex model with disks, arms, Galactic Loop I, and the Local Bubble. The \mathbf{B} model is also the WMAP model (Page et al. 2007),

$$\begin{aligned} \mathbf{B}(\rho, \phi, z) &= b_0 [\cos(\psi(\rho)) \cos(\chi_B(z)) \hat{\rho} \\ &\quad + \sin(\psi(\rho)) \cos(\chi_B(z)) \hat{\phi} + \sin(\chi_B(z)) \hat{z}]. \end{aligned} \quad (13)$$

In this equation, $\{\rho, \phi, z\}$ are the cylindrical coordinates centered at Galactic center and the $\{\hat{\rho}, \hat{\phi}, \hat{z}\}$ are the corresponding unit vectors. For $\rho \in [3, 20]$ kpc, $\psi(\rho) = \psi_0 + \psi_1 \ln(\rho/8 \text{ kpc})$, $\chi_B(z) = \chi_{0,B} \tanh(z/1 \text{ kpc})$. $\psi(\rho)$ and $\chi_B(z)$ are all zero otherwise. The true values of the free parameters in the model are randomly set to $\{b_0, \psi_0, \psi_1, \chi_{0,B}\} = \{1.2 \times 10^{-6} \text{ gauss}, 0.4712 \text{ rad}, 0.0157 \text{ rad}, 0.4363 \text{ rad}\}$. We simulate the maps with $\text{NSIDE} = 64$ and $N_{\text{int}} = 512$, corresponding to a resolution from 0.010 to 0.056 kpc along different LOS. The input for \mathbf{B} and N_0 are callable functions

² <https://blackjax-devs.github.io/blackjax/index.html>

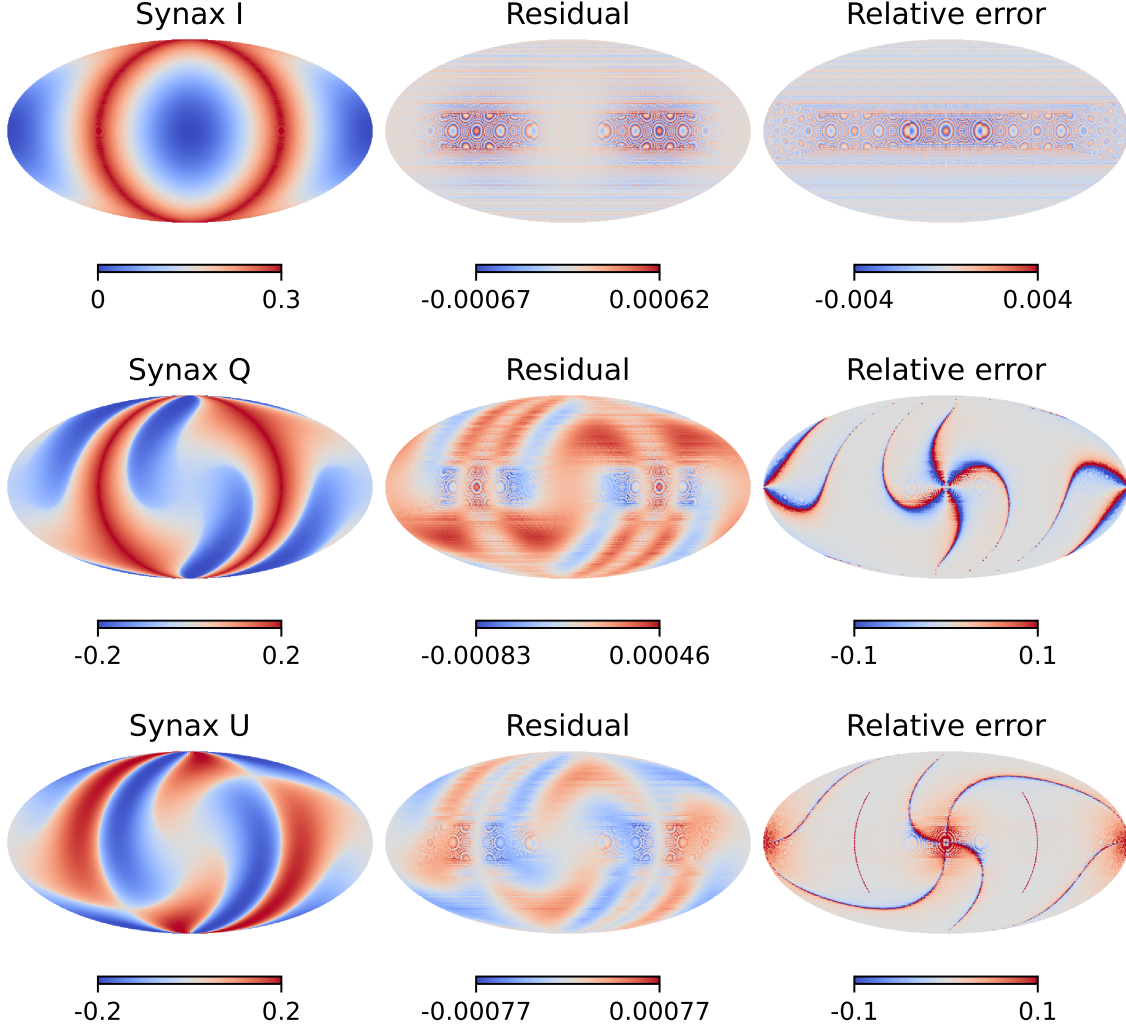


Figure 2. Accuracy test with homogeneous $\{\mathbf{B}(\mathbf{r}), n_e(\mathbf{r}), N_0(\mathbf{r})\}$ fields with callable field generators. The left panel shows the synchrotron $\{I, Q, U\}$ maps generated by *synax*, the middle panel shows the residual between *synax* and theoretical value, and the right panel shows the relative error between *synax* and the theoretical value. Unless mentioned otherwise, all *healpix* maps in this work are in units of Kelvin.

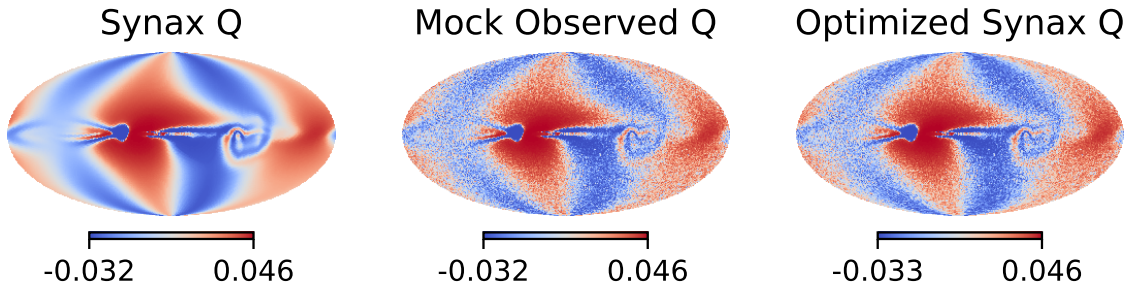


Figure 3. From left to right: simulated synchrotron Q map, mock observation, and optimized synchrotron Q map in units of Kelvin with WMAP \mathbf{B} , N_0 models and YMW16 n_e model at 2.4 GHz. The map has NSIDE = 64 and $N_{\text{int}} = 512$.

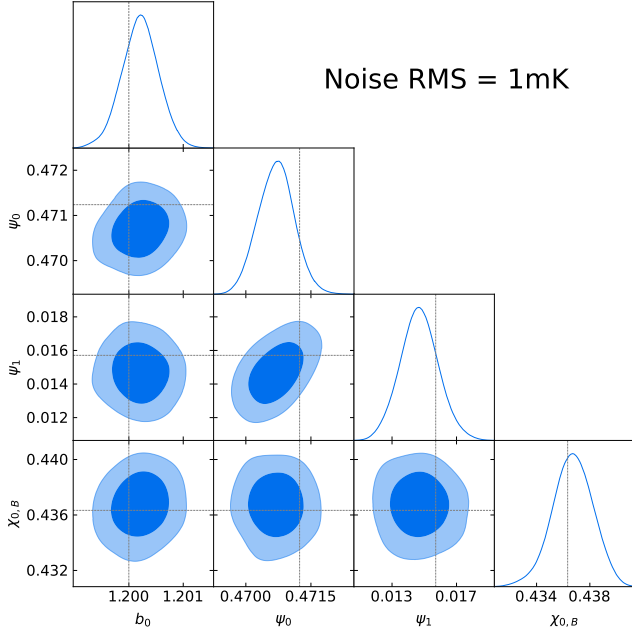


Figure 4. Posteriors for WMAP **B** field parameters with NUTS. The shaded areas are the 1σ (dark blue) and 2σ (light blue) confidence regions, and gray dashed lines indicates the true parameter values. The mock observation map consists of a simulated noiseless map and white noise with standard deviation of 1 mK.

and the n_e input is a 3D grid with resolution (256, 256, 64). The simulated Q map is shown in the left panel of Figure 3. A mock observation is then created by adding Gaussian noise with noise standard deviation $\sigma_n = 1$ mK, as is shown in the middle panel of Figure 3.

We then use `synax` to infer **B**. The n_e and N_0 inputs are identical to the simulation, while we keep $N_{\text{int}} = 512$ to avoid the numerical error from insufficient resolution. We set the prior for these parameters as

$$\begin{aligned} b_0 &\sim \mathcal{U}[0, 10], \\ \psi_0 &\sim \mathcal{U}[0, \pi/2], \\ \psi_1 &\sim \mathcal{U}[0, \pi/2], \\ \chi_{B,0} &\sim \mathcal{U}[0, \pi/2]. \end{aligned} \quad (14)$$

where $\mathcal{U}[a, b]$ represents a flat prior from a to b . The noise in the simulated observations is Gaussian and independent between pixels. The log-likelihood for this model therefore corresponds to the Gaussian likelihood with standard deviation $\sigma = 1$ mK for each pixel,

$$\log \mathcal{L} = \sum_i \left(\frac{(Q_i - Q_{i,\text{obs}})^2}{2\sigma^2} + \frac{(U_i - U_{i,\text{obs}})^2}{2\sigma^2} \right) + C \quad (15)$$

where C is a normalization constant.

3.2. Sampling with NUTS

Table 1. Results of posteriors with NUTS.

Parameter	Best-fit	Accuracy	\hat{r}	ESS
$b_0 [\times 10^{-6} \text{ gauss}]$	1.2002 ± 0.0003	0.01%	1.003	553.35
$\psi_0 [\text{rad}]$	0.4707 ± 0.0004	-0.11%	1.003	503.94
$\psi_1 [\text{rad}]$	0.0147 ± 0.0012	-6.48%	0.999	310.59
$\chi_{0,B} [\text{rad}]$	0.4367 ± 0.0014	0.09%	1.006	252.37

Table 2. ESS per second for NUTS and RWMH after burn-in.

Method	b_0	ψ_0	ψ_1	$\chi_{0,B}$
NUTS GPU	1.90	1.73	1.07	0.87
NUTS CPU	0.09	0.06	0.04	0.03
RWMH GPU	9.49	13.30	7.34	0.37
RWMH CPU	0.14	0.20	0.11	0.01

We first sample the posterior of the WMAP analytical **B** field model parameters, namely $\{b_0, \psi_0, \psi_1, \chi_{0,B}\}$, with NUTS, while other parameters and settings are identical to Section 3.1. We run NUTS for 600 iterations and leave the first 100 as burn-in. Generating a single realization with gradient evaluation requires ~ 100 ms to finish, and such a run takes ~ 7 minutes on an NVIDIA Tesla A100 GPU. The posterior is shown in the left panel of Figure 4. The German-Rubin statistic \hat{r} (Gelman & Rubin 1992) is a convergence diagnostic used in Bayesian statistics to assess the mixing and convergence of MCMC simulations. It compares the variance within and between multiple chains, and its interpretation is closely related to effective sample size (ESS), which quantifies the number of independent samples in correlated chains, providing insight into the quality of the MCMC output. The \hat{r} for the samples are all below 1.01, and the ESS is of the same order as sampling iterations. We can therefore be confident that we have converged on the stationary distribution, and the corresponding posterior samples are generated with minimal auto-correlation. We find the accuracy, defined by $(\bar{p} - p_{\text{true}})/p_{\text{true}}$, is very close to zero, as is listed in Table 1, except for ψ_1 because of its small magnitude. The true parameter mostly lies in the 1σ confidence level of the posterior.

We also run NUTS on CPU and simple Random Walk Metropolis-Hasting MCMCs (RWMH) with GPU and CPU to provide a benchmark, and the ESS per second for each parameter is shown in Table 2. On CPU, a single `synax` realization with 128 threads takes ~ 200 ms to finish. Typically, to ensure convergence, the ESS for all parameters must be beyond a certain threshold. From the comparison of the minimum ESS per second (i.e. ESS per second for $\chi_{0,B}$), we obtain a roughly 20 times speed-up with GPU acceleration, and NUTS brings two times extra improvement in such a simple model. The improvements from using gradient-based

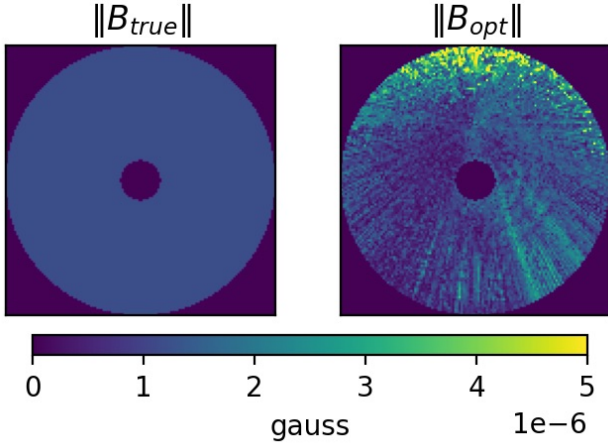


Figure 5. Left: a slice of true \mathbf{B} field magnitude at $z = 0$ kpc. Right: a slice of optimised \mathbf{B} field magnitude at $z = 0$ kpc.

sampling methods such as NUTS will be more apparent for higher dimensional sampling problems (Gelman et al. 1997; Beskos et al. 2013).

3.3. Optimizing 3D Grids

The WMAP analytical modeling of the GMF focuses on the large-scale structure of the Galaxy, but does not account for small-scale features such as turbulence in the Galactic plane. In this work, we consider a more general approach by directly optimizing the 3D \mathbf{B} grids based on mock observations. The grid consists of $128 \times 128 \times 32$ voxels, with a corresponding box size of $(40, 40, 10)$ kpc. Our goal is to optimize the 3D grids to maximize the log-likelihood $\log \mathcal{L}$. Due to the high dimensionality ($\sim 5 \times 10^6$) of this problem, we employ the ADAM optimizer (Kingma & Ba 2014) implemented via Optax (DeepMind et al. 2020)³. To prevent overfitting, optimization is halted after 200 iterations.

The optimized synchrotron map is presented in the right panel of Figure 3. Due to the high flexibility of the grid representation, noise features are also reproduced, indicating significant overfitting. The optimized \mathbf{B} magnitude is shown in Figure 5, where it is evident that the \mathbf{B} field fluctuates considerably to replicate the noise features. Although this result is not physically valid, the striking similarity between the optimized maps and the mock observations demonstrates the model’s ability to reproduce any observation. This also suggests that regularization is required to effectively prevent overfitting when dealing with fields possessing many degrees of freedom.

Moreover, this optimization would be intractable without AD. Traditional methods such as finite difference, exemplified by MIUNIT (James & Roos 1975), are typically used

³ <https://optax.readthedocs.io/en/latest/>

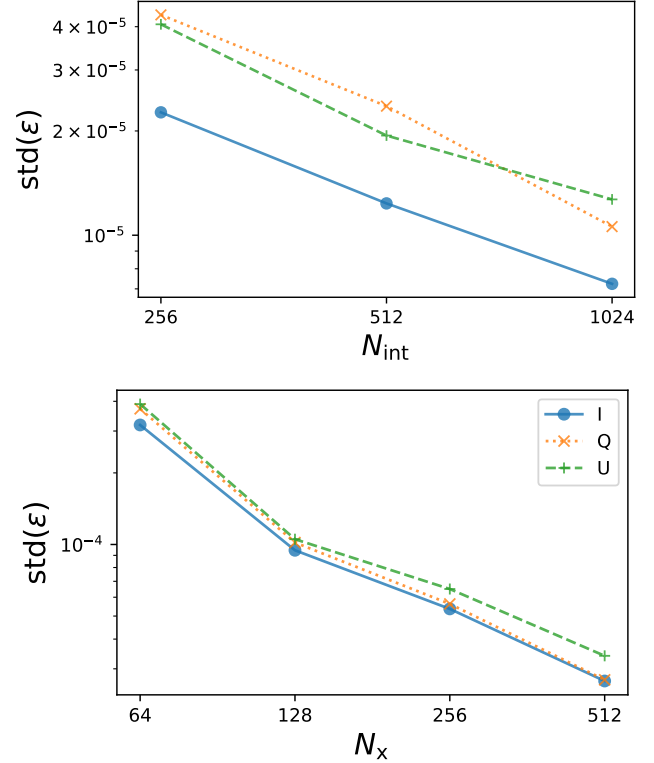


Figure 6. **Upper:** Standard deviation of the residuals for the map with different N_{int} compared to the map with $N_{\text{int}} = 2048$. **Lower:** Standard deviation of the residuals of a grid \mathbf{B} model map compared to an analytical \mathbf{B} model map, as a function of grid size N_x . Solid, dotted, and dashed lines represent $\{I, Q, U\}$ maps respectively.

for optimization tasks (e.g. Unger & Farrar 2024). However, these methods generally require $O(n)$ calls to compute the numerical gradient, where n represents the degrees of freedom. In our field-level optimization problem, $n = 128 \times 128 \times 32$, making the computation of the numerical gradient intractable.

4. DISCUSSION

4.1. Systematics Analysis

In this section, we analyze the errors introduced by numerical methods such as integration and grid interpolation, and we fix NSIDE = 64 in this subsection. First, we explore the integration error by varying the number of integration points, $N_{\text{int}} = 256, 512, 1024, 2048$, which corresponds to a maximum resolution ranging from 0.13 to 0.02 kpc. All other hyperparameters and physical models are kept identical to those described in Section 3.1. The systematic error is evaluated by calculating the standard deviation of the residuals relative to the $N_{\text{int}} = 2048$ map, defined as $\text{std}(\epsilon) = \text{std}(\text{Map}_{N_{\text{int}}} - \text{Map}_{2048})$. The variation of $\text{std}(\epsilon)$ with N_{int} is depicted in the upper panel of Figure 6. We find that the typical scale of systematic errors is less than 4×10^{-5} K, even with $N_{\text{int}} = 256$, which is significantly be-

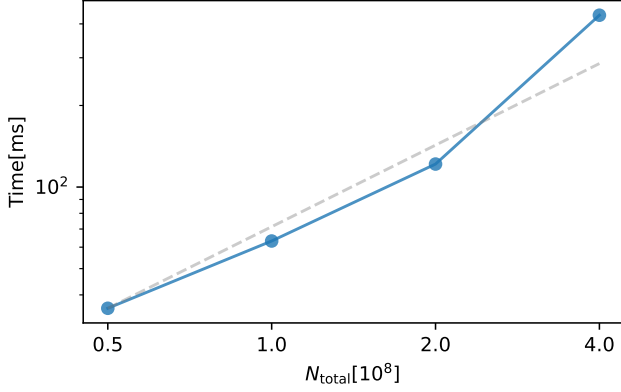


Figure 7. The blue solid line indicates wall time for a single realization with respect to the total number of integration points N_{total} with Tesla A100 GPU. The grey dotted line corresponds to theoretical scaling where time is proportional to N_{total} .

low the 1 mK sensitivity of the 2.3 GHz S-PASS survey (e.g. [Krachmalnicoff et al. 2018](#)), which we treat as typical for the frequency range we consider. Consequently, it is safe to use a relatively smaller N_{int} to expedite the inference process, and these systematics can be safely ignored when evaluating the likelihood.

Secondly, we assess the error associated with using 3D grid and interpolation functions as field generators. The fiducial model in this analysis is identical to that described in Section 3.1. To evaluate the interpolation error, we first generate a \mathbf{B} field on regular grids of size $(N_x, N_x, N_x/4)$ using the WMAP analytical function and then interpolate these fields to the desired integration points to calculate the resulting synchrotron emission. We choose N_x to be 64, 128, 256, 512. The systematic error is characterized by $\text{std}(\epsilon) = \text{std}(\text{Map}_{N_x} - \text{Map}_{\text{ana}})$, where Map_{ana} represents the synchrotron map generated using the analytical expression, which serves as our fiducial model, and N_{int} is fixed as 512. The results is shown at the lower panel of Figure 6. We observe that with $N_x = 64$, the error reaches sub-mK levels, making it non-negligible during the inference process. As the grid size increases, the error level decreases to 10^{-5} K with $N_x = 512$, indicating an insignificant contribution from interpolation. However, it is important to note that the fiducial model here assumes a smooth \mathbf{B} field, which reduces the interpolation error. A higher level of systematic error is possible with a turbulent \mathbf{B} field with low smoothness, especially when using smaller N_x values.

4.2. Detailed Performance profiling

We then analyze the time elapsed for carrying out one simulation with different numbers of total integration points N_{total} . The number N_{total} can be evaluated using $N_{\text{total}} = 12 \times \text{NSIDE}^2 \times N_{\text{int}}$, and $\text{NSIDE} = 128$ here. Ideally, the runtime should be proportional to N_{total} since the op-

Table 3. Model parameters for four WMAP \mathbf{B} field models in the 16-parameter model analysis.

Model	$b_0 [\times 10^{-6} \text{ gauss}]$	$\psi_0 [\text{rad}]$	$\psi_1 [\text{rad}]$	$\chi_{0,B} [\text{rad}]$
Model 1	1.20	0.4712	0.0157	0.4363
Model 2	3.50	0.6457	0.5393	0.6108
Model 3	7.70	1.1693	1.0629	1.1344
Model 4	5.70	1.6930	1.5865	1.6580

erations in any integration point have constant computational complexity. We change N_{total} by setting different $N_{\text{int}} = \{256, 512, 1024, 2048\}$, and the corresponding runtime is shown in Figure 7. We find that the actual runtime has a similar trend to the theoretical scaling, indicating the workload is equally distributed to GPU cores, and the utilization is nearly optimal.

For $N_{\text{total}} > 10^8$, the runtime of a single realization exceeds ~ 50 ms. Although evaluating the gradient at least doubles the runtime and enters the regime of expensive models, this additional computational cost is justified by the ability to employ gradient-based inference algorithms, which scale more effectively with dimensionality, and fully leverage the parallel computation capabilities of GPUs and TPUs.

4.3. Sampling with a 16-parameter model

To assess the performance of *synax* with gradient-based sampling methods with higher dimensions, we construct a mock observation using a 16-parameter model. This model is based on four WMAP magnetic field configurations, denoted as $\{\mathbf{B}_1, \mathbf{B}_2, \mathbf{B}_3, \mathbf{B}_4\}$, each characterized by different parameter sets shown in Table 3. The total magnetic field, $\mathbf{B}_{\text{total}}$, is generated by stacking these components with randomly chosen weights,

$$\begin{aligned} \mathbf{B}_{\text{total}} = & (0.6B_{1,x} + 0.3B_{2,x} + 0.1B_{3,z} + 0.3B_{4,y})\hat{x} \\ & + (0.6B_{1,y} + 0.3B_{2,z} + 0.1B_{3,y} + 0.3B_{4,x})\hat{y} \\ & + (0.6B_{1,z} + 0.3B_{2,y} + 0.1B_{3,x} + 0.3B_{4,z})\hat{z} \end{aligned} \quad (16)$$

Here, $\{B_{*,x}, B_{*,y}, B_{*,z}\}$ represent the three components of the magnetic field, while $\{\hat{x}, \hat{y}, \hat{z}\}$ are unit vectors along the respective axes. To avoid multimodality in the posterior distribution, $\{\mathbf{B}_2, \mathbf{B}_3, \mathbf{B}_4\}$ are rotated before stacking. Other fields and a noisy mock observation is then generated using the same model described in Section 3.

We compare the performance of the NUTS and RWMH algorithms on GPU for sampling this more complex model. NUTS achieves a minimum ESS per second of 1.53×10^{-2} , whereas RWMH fails to converge within 12 hours, demonstrating the clear advantage of NUTS for efficiently exploring high-dimensional parameter spaces.

4.4. Reproducing the Haslam Map

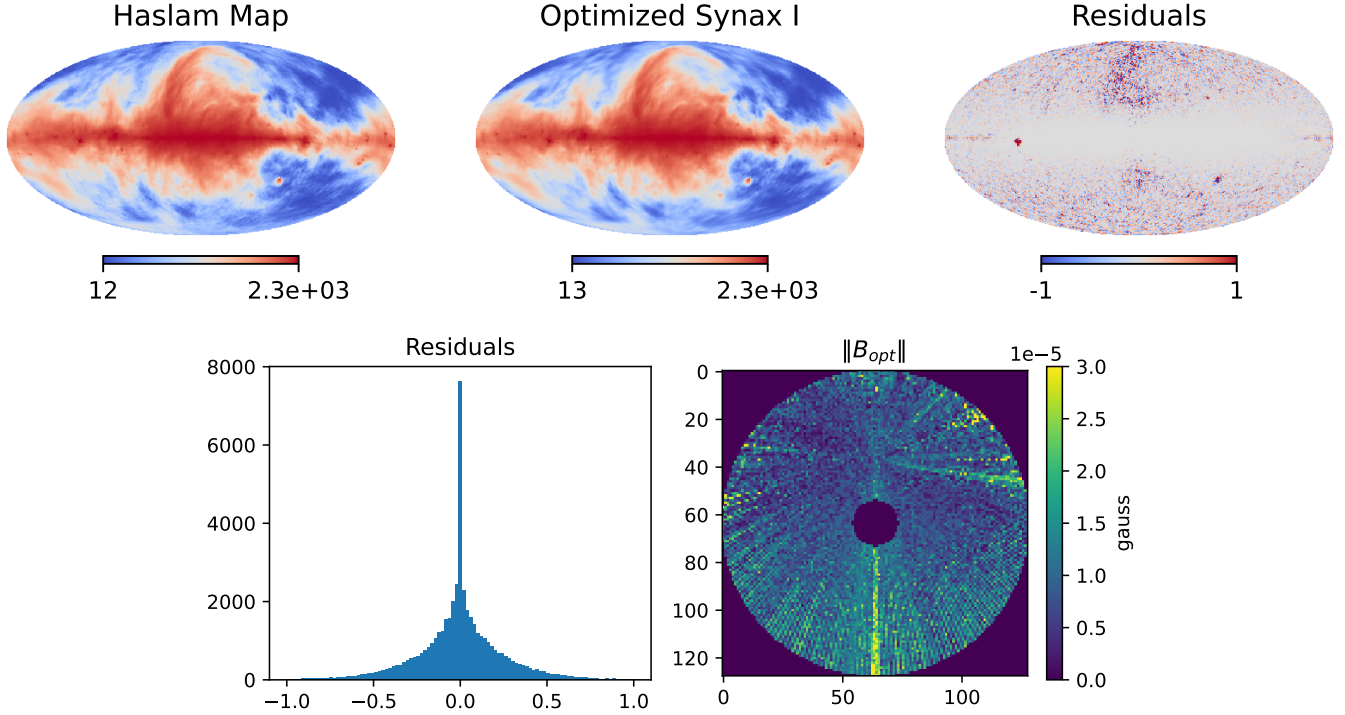


Figure 8. Reproduced Haslam map by optimising the \mathbf{B} field on grids in units of Kelvin. *Top left:* Haslam map spatially averaged to NSIDE = 64. *Top middle:* Synchrotron I map generated with optimized \mathbf{B} field. *Top right:* residual map of the optimised I map compared with Haslam map. *Bottom left:* histogram of residuals. *Bottom right:* a slice of optimised \mathbf{B} magnitude at $z=0$ kpc.

To test the performance of our code in a more complex and realistic situation, we optimize the 3D \mathbf{B} field on grids to generate a simulation based on the Haslam map⁴ (Remazeilles et al. 2015). We downgrade the map to NSIDE = 64 by spatial averaging and neglect the beam effect since the pixel size is approximately equivalent to the Haslam beam with FWHM = 56 arcmin. We use the identical settings to Section 3.3. The results are shown in Figure 8. The optimized \mathbf{B} field faithfully reproduces the Haslam map, with a residual standard deviation of 0.29 K. We see from the residual map that, except for some bright spots that are likely to be localized objects, the reconstruction error is very close to zero. However, the optimized $\|\mathbf{B}\|$ shows radial features, indicating strong degeneracy along the LoS direction. We expect additional modeling and data in intensity and polarization to break the degeneracy in future work.

5. CONCLUSION

In this paper, we introduce *synax*, a novel synchrotron intensity and polarization simulation package that leverages AD and hardware acceleration for the first time. GPU acceleration significantly enhances computational speed, while AD enables efficient sampling algorithms for Bayesian posterior

inference. The full 3D representation of fields within AD-based optimization algorithms allows for the characterization of more complex Galactic field structures.

We validate the accuracy of *synax*, demonstrating that the error budget remains below 1 mK in our test scenarios. Utilizing a mock observation based on the four-parameter WMAP GMF model, we evaluate the efficiency of NUTS in obtaining parameter posteriors. Our results show a twenty-fold increase in computational efficiency due to GPU acceleration and an additional two-fold improvement in sampling efficiency with NUTS compared to the RWMH method in a four-parameter model, as evidenced by the ESS metric. On a more complex 16-parameter model, RWMH does not converge, while NUTS with *synax* report an ESS per second of 1.53×10^{-2} . Furthermore, we test the use of 3D grids for field representation, finding that while the 3D field reproduces the mock observation with high fidelity, it introduces a significant bias, indicating the need for further regularization.

We conduct a detailed analysis of accuracy and performance, beginning with errors arising from insufficient integration step sizes. We find that the standard deviation of the error remains well below the millikelvin level for maximum step sizes under 0.13 kpc. Similarly, interpolation errors with 3D grid representations maintain similar accuracy for grid resolutions below 0.08 kpc. In terms of runtime, *synax* can

⁴ https://lambda.gsfc.nasa.gov/product/foreground/fg_2014_haslam_408_get.html

produce a map with 5×10^8 integration points in approximately 300 ms on an NVIDIA A100 GPU.

As future radio observations targeting from the 21 cm to CMB polarization aim at increasingly precise measurements, a deeper understanding of Galactic structure is crucial, both for elucidating Galactic evolution and for mitigating foreground contamination in cosmological signals. *synax* facilitates rapid inference with complex models, contributing to a more precise understanding of the Galaxy.

In this work, we neglect secondary effects such as self-absorption and conversion (e.g. Jones & O’Dell 1977; Chan et al. 2019) which will be addressed in future updates. Additionally, while free-free emission and absorption—negligible beyond the GHz range—are not considered here, they play a critical role in low-frequency observations, which are essential for probing the early Uni-

verse. Future iterations of *synax* will include these processes to extend its applicability to the low-frequency domain.

1 KND, RDPG and YM are supported by the National SKA
2 Program of China (grant No. 2020SKA0110401) and NSFC
3 (grant No. 11821303). This work is also supported by U.S.
4 Department of Energy, Office of Science, Office of Advanced
5 Scientific Computing Research under Contract No. DE-
6 AC02-05CH11231 at Lawrence Berkeley National Labora-
7 tory to enable research for Data-intensive Machine Learning
8 and Analysis.

Software: JAX (DeepMind et al. 2020), Optax, blackjax (Cabezas et al. 2024), healpy (Zonca et al. 2019; Górski et al. 2005), hamurabi (Waelkens et al. 2009; Wang et al. 2020), numpyro (Phan et al. 2019; Bingham et al. 2019).

REFERENCES

- Adriani, O., Barbarino, G. C., Bazilevskaya, G. A., et al. 2011, *PhRvL*, 106, 201101, doi: [10.1103/PhysRevLett.106.201101](https://doi.org/10.1103/PhysRevLett.106.201101)
- Bennett, C. L., Hill, R. S., Hinshaw, G., et al. 2003, *ApJS*, 148, 97, doi: [10.1086/377252](https://doi.org/10.1086/377252)
- Beskos, A., Pillai, N., Roberts, G., Sanz-Serna, J.-M., & Stuart, A. 2013, *Bernoulli*, 19, 1501. <http://www.jstor.org/stable/42919328>
- Betancourt, M. 2017, arXiv e-prints, arXiv:1701.02434, doi: [10.48550/arXiv.1701.02434](https://doi.org/10.48550/arXiv.1701.02434)
- Bingham, E., Chen, J. P., Jankowiak, M., et al. 2019, *J. Mach. Learn. Res.*, 20, 28:1. <http://jmlr.org/papers/v20/18-403.html>
- Cabezas, A., Corenflos, A., Lao, J., & Louf, R. 2024, *BlackJAX: Composable Bayesian inference in JAX*. <https://arxiv.org/abs/2402.10797>
- Chan, J. Y. H., Wu, K., On, A. Y. L., et al. 2019, *MNRAS*, 484, 1427, doi: [10.1093/mnras/sty3498](https://doi.org/10.1093/mnras/sty3498)
- Cong, Y., Yue, B., Xu, Y., et al. 2021, *ApJ*, 914, 128, doi: [10.3847/1538-4357/abf55c](https://doi.org/10.3847/1538-4357/abf55c)
- Cong, Y., Yue, B., Xu, Y., Shi, Y., & Chen, X. 2022, *ApJ*, 940, 180, doi: [10.3847/1538-4357/ac9df7](https://doi.org/10.3847/1538-4357/ac9df7)
- DeepMind, Babuschkin, I., Baumli, K., et al. 2020, *The DeepMind JAX Ecosystem*. <http://github.com/google-deeppmind>
- Drimmel, R., & Spergel, D. N. 2001, *ApJ*, 556, 181, doi: [10.1086/321556](https://doi.org/10.1086/321556)
- Drury, L. O. 1983, *Reports on Progress in Physics*, 46, 973, doi: [10.1088/0034-4885/46/8/002](https://doi.org/10.1088/0034-4885/46/8/002)
- Eriksen, H. K., Dickinson, C., Jewell, J. B., et al. 2008, *The Astrophysical Journal*, 672, L87–L90, doi: [10.1086/526545](https://doi.org/10.1086/526545)
- Gaisser, T. K., Stanev, T., & Tilav, S. 2013, *Frontiers of Physics*, 8, 748, doi: [10.1007/s11467-013-0319-7](https://doi.org/10.1007/s11467-013-0319-7)
- Gelman, A., Gilks, W. R., & Roberts, G. O. 1997, *The annals of applied probability*, 7, 110
- Gelman, A., & Rubin, D. B. 1992, *Statistical Science*, 7, 457, doi: [10.1214/ss/1177011136](https://doi.org/10.1214/ss/1177011136)
- Gong, Y., Silva, M., Cooray, A., & Santos, M. G. 2014, *ApJ*, 785, 72, doi: [10.1088/0004-637X/785/1/72](https://doi.org/10.1088/0004-637X/785/1/72)
- Górski, K. M., Hivon, E., Banday, A. J., et al. 2005, *ApJ*, 622, 759, doi: [10.1086/427976](https://doi.org/10.1086/427976)
- Hoffman, M. D., & Gelman, A. 2011, arXiv e-prints, arXiv:1111.4246, doi: [10.48550/arXiv.1111.4246](https://doi.org/10.48550/arXiv.1111.4246)
- James, F., & Roos, M. 1975, *Computer Physics Communications*, 10, 343, doi: [10.1016/0010-4655\(75\)90039-9](https://doi.org/10.1016/0010-4655(75)90039-9)
- Jansson, R., & Farrar, G. R. 2012, *ApJL*, 761, L11, doi: [10.1088/2041-8205/761/1/L11](https://doi.org/10.1088/2041-8205/761/1/L11)
- Jones, M. E., Taylor, A. C., Aich, M., et al. 2018, *MNRAS*, 480, 3224, doi: [10.1093/mnras/sty1956](https://doi.org/10.1093/mnras/sty1956)
- Jones, T. W., & O’Dell, S. L. 1977, *ApJ*, 214, 522, doi: [10.1086/155278](https://doi.org/10.1086/155278)
- Kingma, D. P., & Ba, J. 2014, arXiv e-prints, arXiv:1412.6980, doi: [10.48550/arXiv.1412.6980](https://doi.org/10.48550/arXiv.1412.6980)
- Krachmalnicoff, N., Carretti, E., Baccigalupi, C., et al. 2018, *A&A*, 618, A166, doi: [10.1051/0004-6361/201832768](https://doi.org/10.1051/0004-6361/201832768)
- Liu, A., & Shaw, J. R. 2020, *PASP*, 132, 062001, doi: [10.1088/1538-3873/ab5bfd](https://doi.org/10.1088/1538-3873/ab5bfd)
- Maniyar, A. S., Gkogkou, A., Coulton, W. R., et al. 2023, *PhRvD*, 107, 123504, doi: [10.1103/PhysRevD.107.123504](https://doi.org/10.1103/PhysRevD.107.123504)
- Page, L., Hinshaw, G., Komatsu, E., et al. 2007, *ApJS*, 170, 335, doi: [10.1086/513699](https://doi.org/10.1086/513699)
- Phan, D., Pradhan, N., & Jankowiak, M. 2019, arXiv preprint arXiv:1912.11554
- Planck Collaboration, Adam, R., Ade, P. A. R., et al. 2016a, *A&A*, 596, A104, doi: [10.1051/0004-6361/201628522](https://doi.org/10.1051/0004-6361/201628522)
- , 2016b, *A&A*, 594, A10, doi: [10.1051/0004-6361/201525967](https://doi.org/10.1051/0004-6361/201525967)

- Planck Collaboration, Akrami, Y., Ashdown, M., et al. 2020, *A&A*, 641, A4, doi: [10.1051/0004-6361/201833881](https://doi.org/10.1051/0004-6361/201833881)
- Remazeilles, M., Dickinson, C., Banday, A. J., Bigot-Sazy, M. A., & Ghosh, T. 2015, *MNRAS*, 451, 4311, doi: [10.1093/mnras/stv1274](https://doi.org/10.1093/mnras/stv1274)
- Rubiño-Martín, J. A., Guidi, F., Génova-Santos, R. T., et al. 2023, *MNRAS*, 519, 3383, doi: [10.1093/mnras/stac3439](https://doi.org/10.1093/mnras/stac3439)
- Rybicki, G. B., & Lightman, A. P. 1986, *Radiative Processes in Astrophysics* (New York: Wiley)
- Strong, A. W., Moskalenko, I. V., & Ptuskin, V. S. 2007, *Annual Review of Nuclear and Particle Science*, 57, 285, doi: [10.1146/annurev.nucl.57.090506.123011](https://doi.org/10.1146/annurev.nucl.57.090506.123011)
- Unger, M., & Farrar, G. R. 2024, *ApJ*, 970, 95, doi: [10.3847/1538-4357/ad4a54](https://doi.org/10.3847/1538-4357/ad4a54)
- Waelkens, A., Jaffe, T., Reinecke, M., Kitaura, F. S., & Enßlin, T. A. 2009, *A&A*, 495, 697, doi: [10.1051/0004-6361:200810564](https://doi.org/10.1051/0004-6361:200810564)
- Wang, J., Jaffe, T. R., Enßlin, T. A., et al. 2020, *ApJS*, 247, 18, doi: [10.3847/1538-4365/ab72a2](https://doi.org/10.3847/1538-4365/ab72a2)
- West, J. L., Jaffe, T., Ferrand, G., Safi-Harb, S., & Gaensler, B. M. 2017, *ApJL*, 849, L22, doi: [10.3847/2041-8213/aa94c4](https://doi.org/10.3847/2041-8213/aa94c4)
- Yan, H., & Lazarian, A. 2008, *ApJ*, 673, 942, doi: [10.1086/524771](https://doi.org/10.1086/524771)
- Yao, J. M., Manchester, R. N., & Wang, N. 2017, *ApJ*, 835, 29, doi: [10.3847/1538-4357/835/1/29](https://doi.org/10.3847/1538-4357/835/1/29)
- Zonca, A., Singer, L., Lenz, D., et al. 2019, *Journal of Open Source Software*, 4, 1298, doi: [10.21105/joss.01298](https://doi.org/10.21105/joss.01298)